Electronic Supplementary Material (ESI) for Journal of Materials Chemistry C.

Supplementary Information

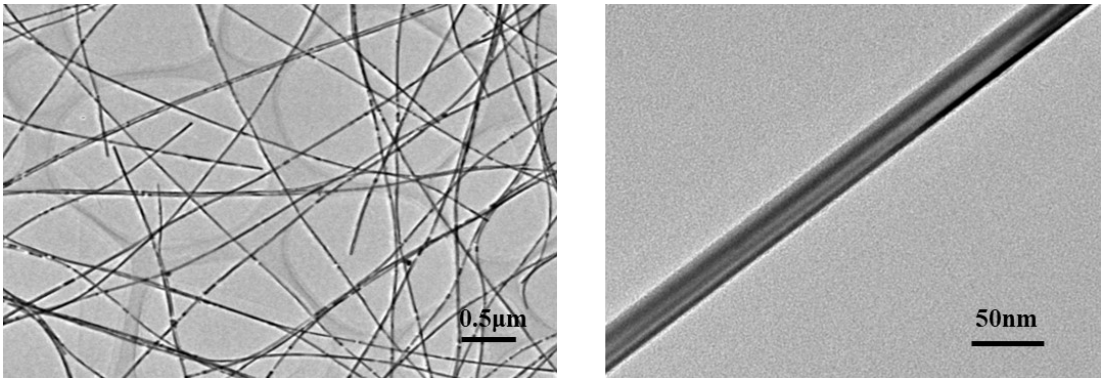

Figure S1 TEM images of AgNWs with a diameter of 30 nm.

Fig. S1 shows the TEM images of AgNWs, and it is observed that AgNWs exhibit a diameter of 30 nm, which is suitable for high-performance TCFs.

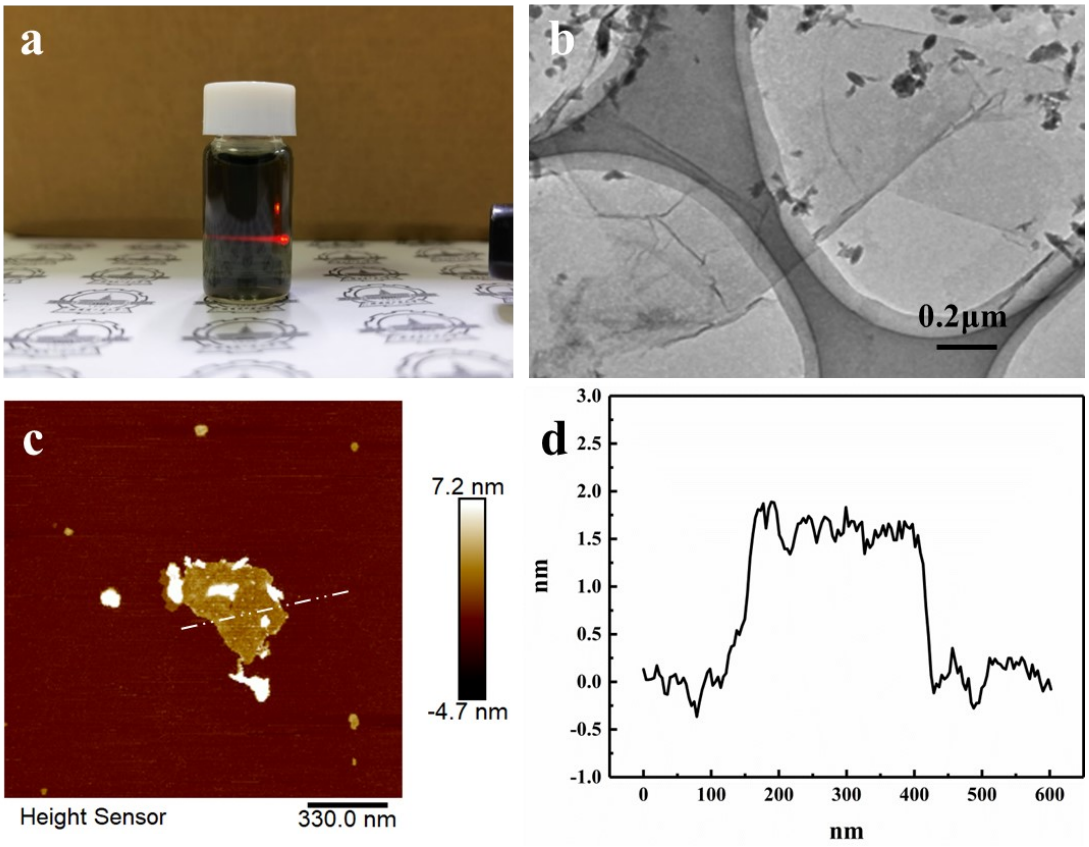

Figure S2 a: Tyndall scattering effect, b: TEM images and c: AFM images of $Ti_3C_2T_x$ MXene nanosheet, d: Thickness characterization of $Ti_3C_2T_x$ MXene nanosheets.

MXene nanosheets dispersed in DI water form a uniform colloidal solution by the Tyndall scattering effect shown in Fig. S2a. The TEM image exhibits the structure of a single-layer MXene nanosheet with an average size of greater than 500 nm. AFM images show that the thickness of the monolayer MXene is 1.5-2 nm. AgNW and MXene are suitable for TCFs because of the high transparency in the visible region.

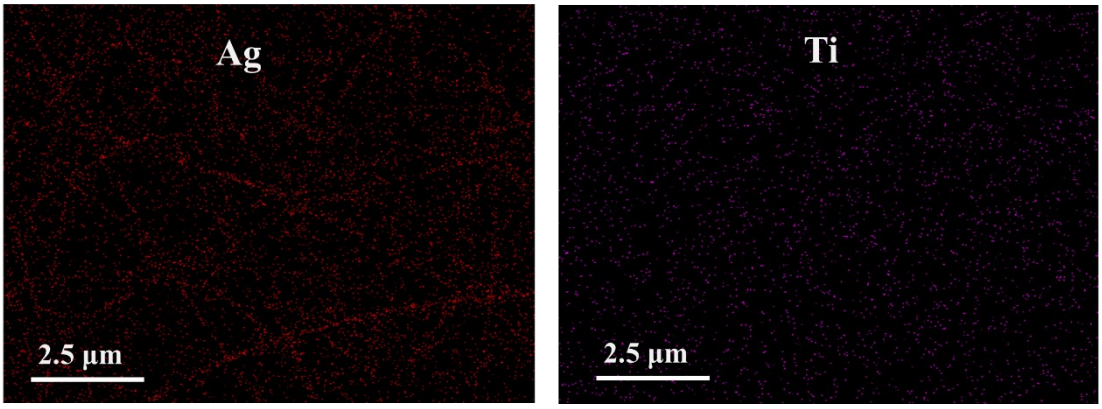

Figure S3 EDS mapping of AgNW-MXene/PU TCFs.

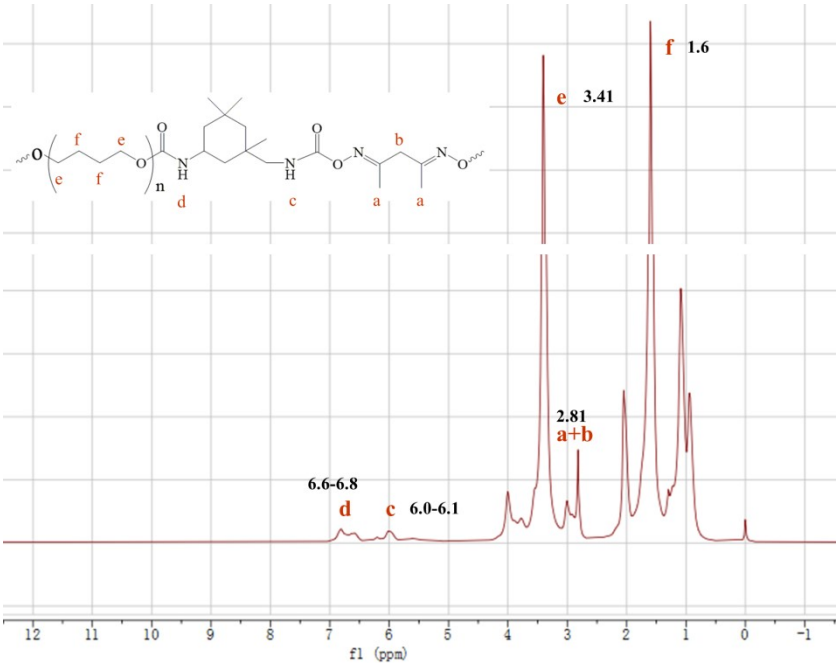

Figure S4. ^{1}HNMR chemical shift of PU-DMBA$_{0.25}$

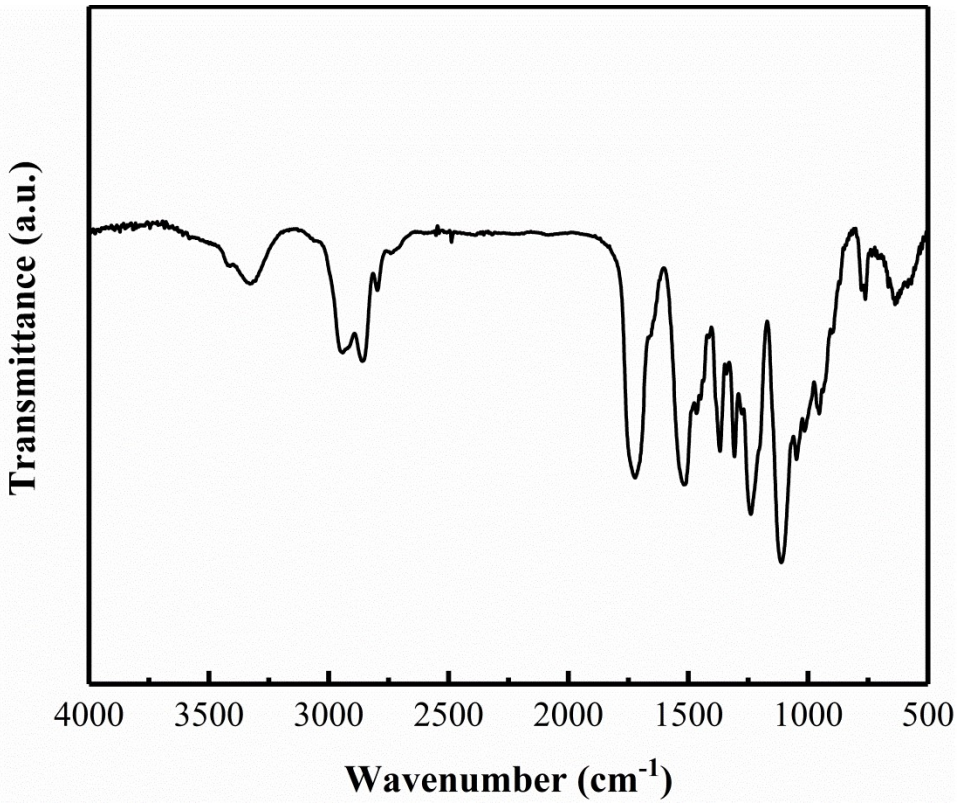

Figure S5. FTIR spectrum in the range of 4000–500 cm^{-1} for the PU-$DMBA_{0.25}$ elastomer.

Table S1. Characteristic peak assignments of the PU-$DMBA_{0.25}$ elastomer.

Assignments	Wavenumber (cm^{-1})
free ν (N-H)	3421
H-bonded ν (N-H)	3327
ν_a (CH_2)	2947
ν_a (CH_2)	2911
ν_s (CH_2)	2859
ν_s (CH_2)	2798
free ν (C=O) amide I	1725
H-bonded ν (C=O) amide I	1700
H-bonded ν (C-N) + δ (N-H) amide II	1536
free ν (C-N) + δ (N-H) amide II	1502
H-bonded ν (C-N) + δ (N-H) amide III	1247
free ν (C-N) + δ (N-H) amide III	1223
ν (C-O-C)	1110

Table S2. Mechanical properties, self-healing efficiency (SE), and η of the PU-DMBA$_{0.25}$ elastomer healed at different temperatures for 12 h.

Temp. (°C)	Tensile strength (MPa)	Elongation (%)	Tensile strength SE (%)	Elongation SE (%)	η (%)
Raw	24.4	1411.2	/	/	/
25	4.9	372.0	20.1	26.3	10.1
60	16.4	1121.5	67.2	79.5	60.5
70	23.5	1347.7	96.3	95.5	93.3

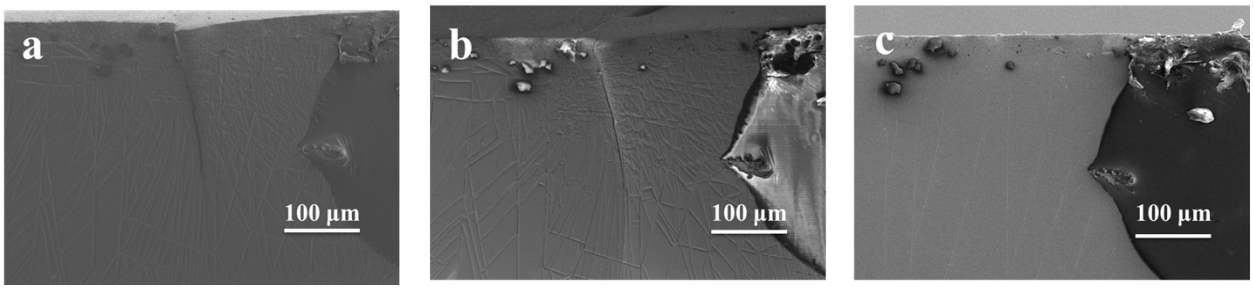

Figure S6 Cross-sectional SEM images of incision sections, the PU-DMBA$_{0.25}$ is cut to form a crack on the surface (a) and then heated at 70 °C for 3 min (b) and 5 min (c).

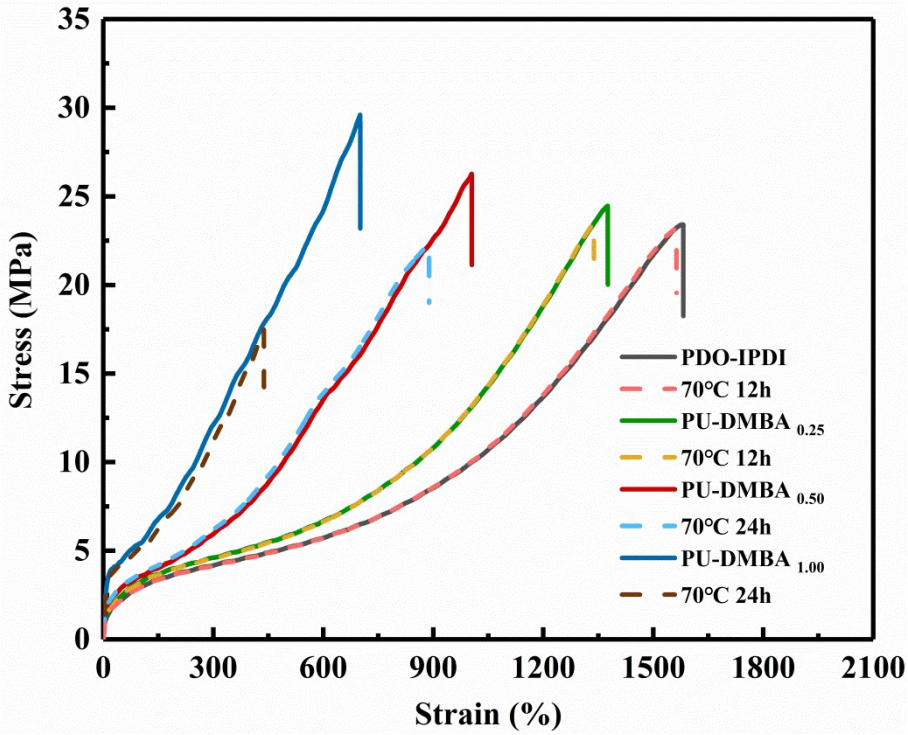

Figure S7 Stress-strain curves of all elastomers before and after self-healing.

The self-healing efficiency of the elastomer decreases with increasing *x*, and when the value of *x* is greater than 0.5, the self-healing efficiency is not significantly improved even if the heating time is extended to 24 h.

Table S3. Mechanical properties and η values of other elastomers.

Sample	Tensile strength (MPa)	Elongation (%)	η (%)	Healing condition
PDO-IPDI	23.5	1578.7	97.6	70 °C/12 h
PU-DMBA$_{0.50}$	26.2	1002.6	78.6	70 °C/24 h
PU-DMBA$_{1.00}$	29.6	700.0	37.9	70 °C/24 h

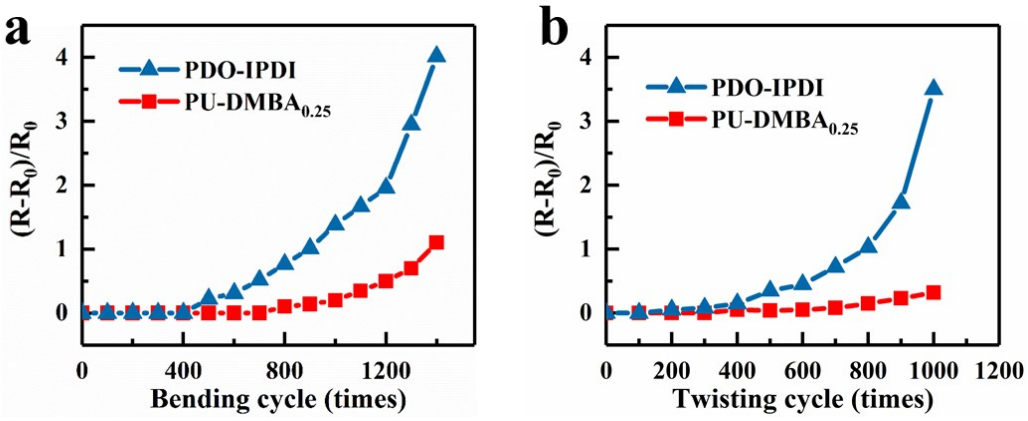

Figure S8 Sheet resistance after 1400 bending (a) and 1000 twisting (b) cycles for PDO-IPDI and PU-DMBA$_{0.25}$-based TCFs.

Bending and twisting tests were used to evaluate the mechanical stability of the TCF. A sample with a length of 4 mm was bent on a universal electronic tensile testing machine along the length until both ends contacted, repeating the cycle for 1400 times to test the bending properties of the material. The twisting test was performed on a two-axis fatigue testing machine by fixing one end and twisting the other end around the axial direction by 90° for 1000 repetitive cycles. In both of these processes, the sheet resistance of the sample was recorded every 100 times; three measurements were performed each time and the results were then averaged. Clearly, the PDO-IPDI without DMBA control group has poor resistance to bending, and the sheet resistance changed significantly after 400 bending cycles. However, when x was increased to 0.25, the flexural resistance of the composite changed significantly and the composite was able to withstand 1000 bending cycles. Similarly, PU-DMBA$_{0.25}$ exhibited excellent stability in the twisting test, exhibiting relatively low resistance change during the twisting test after over 1000 cycles.

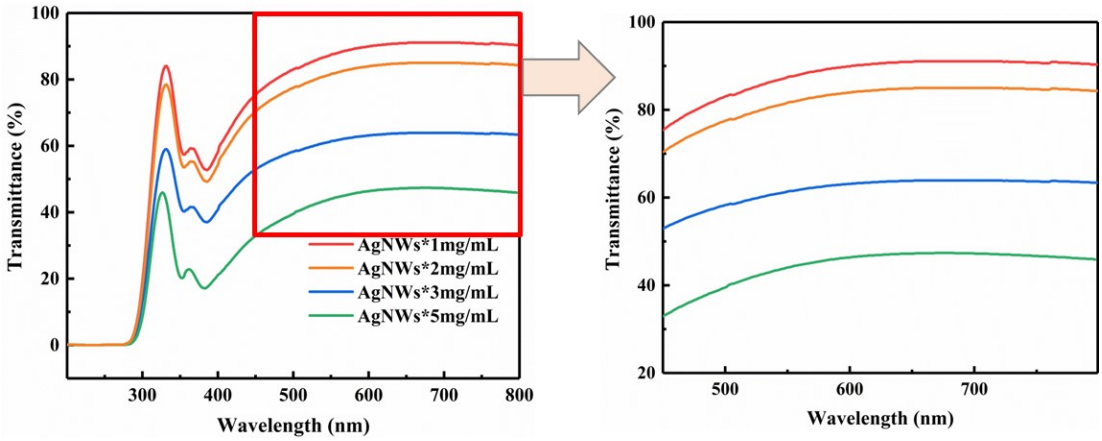

Figure S9 Visible light transmittance of AgNWs deposited on PU-DMBA$_{0.25}$ at different concentrations.

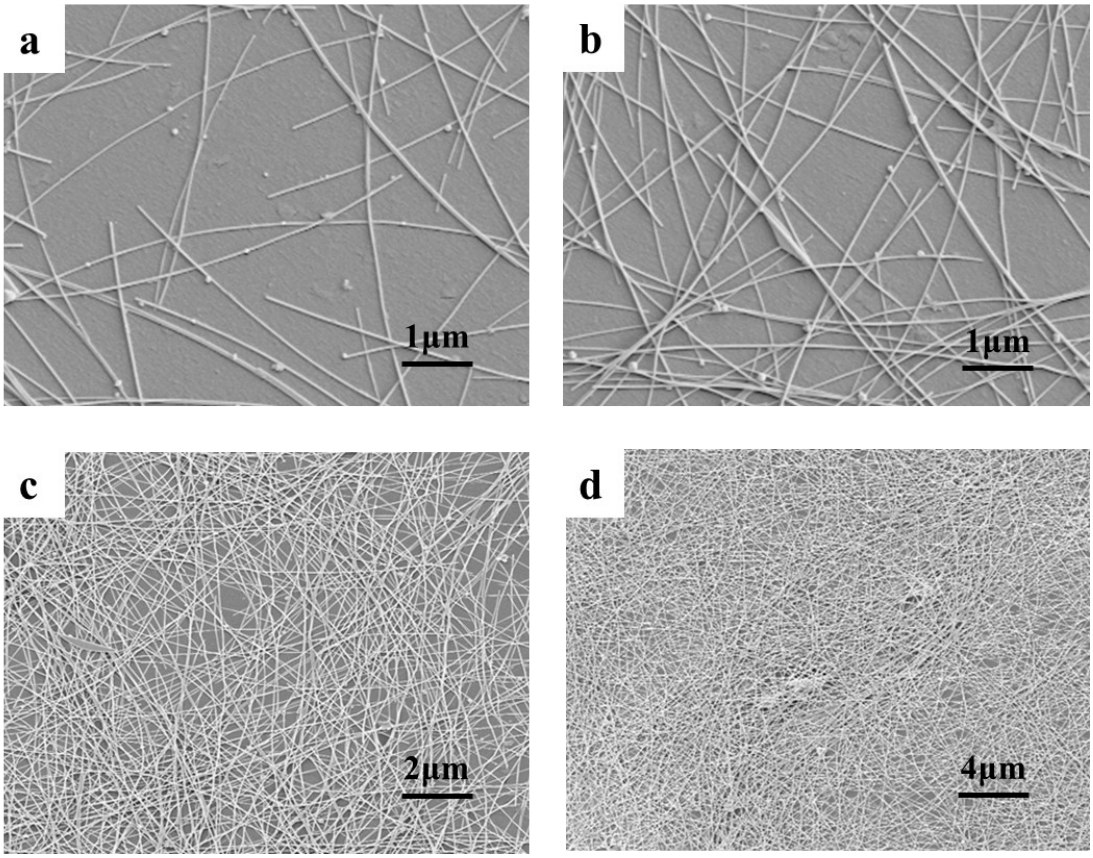

Figure S10 SEM images of blade-coated AgNWs with a: 1mg/mL, b: 2mg/mL, c: 3mg/mL, d: 5mg/mL concentrations on the PU-$DMBA_{0.25}$.

It can be clearly seen that when the concentration of the AgNWs solution is increased to 3 mg/mL, the silver nanowires begin to stack with each other, affecting the transmittance of the film.

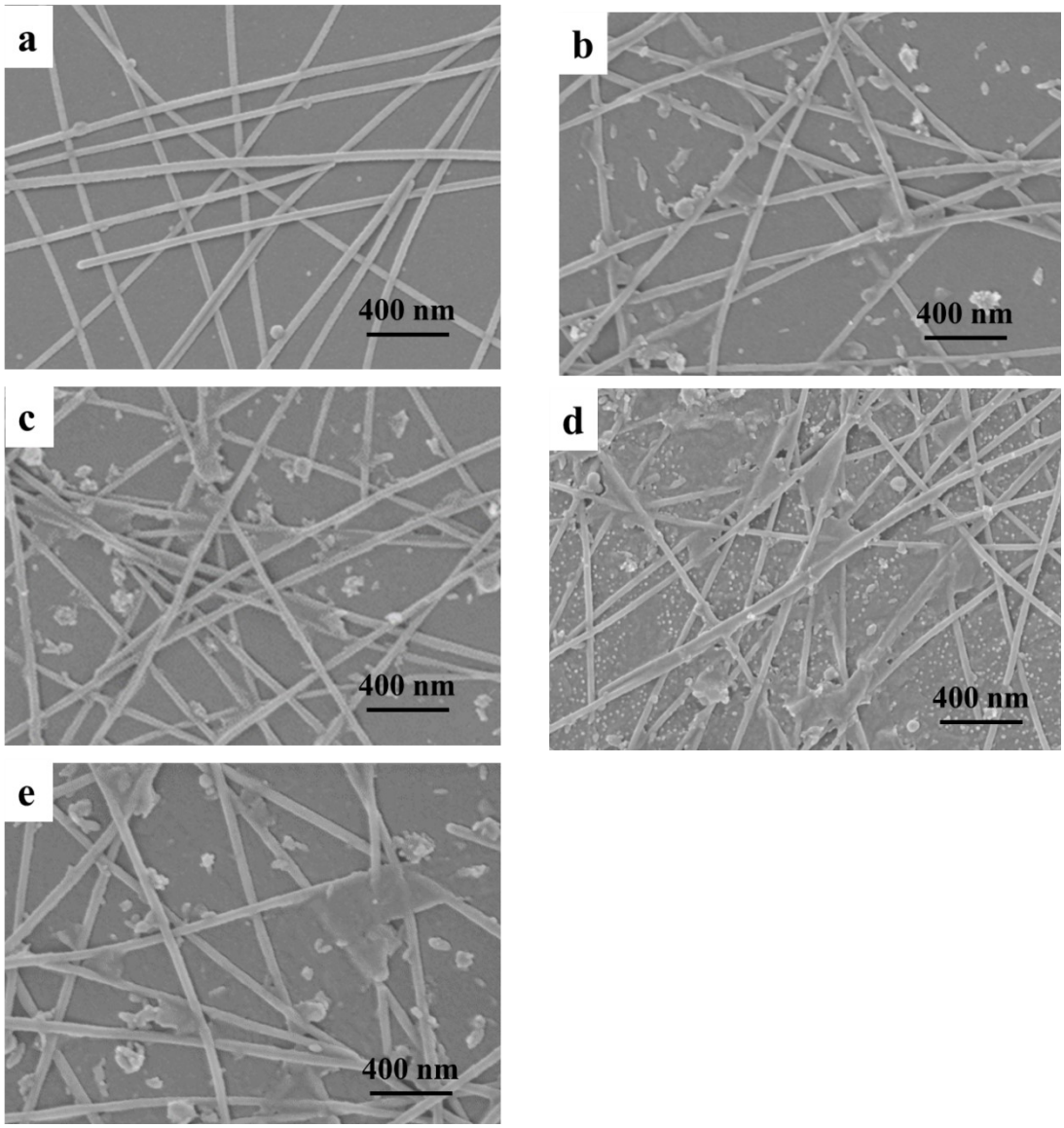

Figure S11 SEM images of spin-coating MXene with a: 0 mg/mL (2 mg/mL of AgNWs), b: 0.2 mg/mL, c: 0.4 mg/mL, d: 0.6 mg/mL, e: 0.8 mg/mL concentrations on the 2 mg/mL of AgNWs coated PU-$DMBA_{0.25}$.

The self-healing efficiency of the electrical conductivity (η_e) was calculated using Eq. (S1) as follows:

$$\eta_e = \frac{EMI\ SE_h}{EMI\ SE_o} \times 100\% \quad \text{(S1)}$$

where EMI SE_h and EMI SE_o correspond to the electromagnetic interference shielding effectiveness of healed and original samples, respectively.

Table S4. Self-healing efficiency of the electrical conductivity of AgNW-MXene/PU-$DMBA_{0.25}$ TCF.

Healing times	Original	1st	2nd	3rd
η_e (%)	-	99.2	97.7	95.2

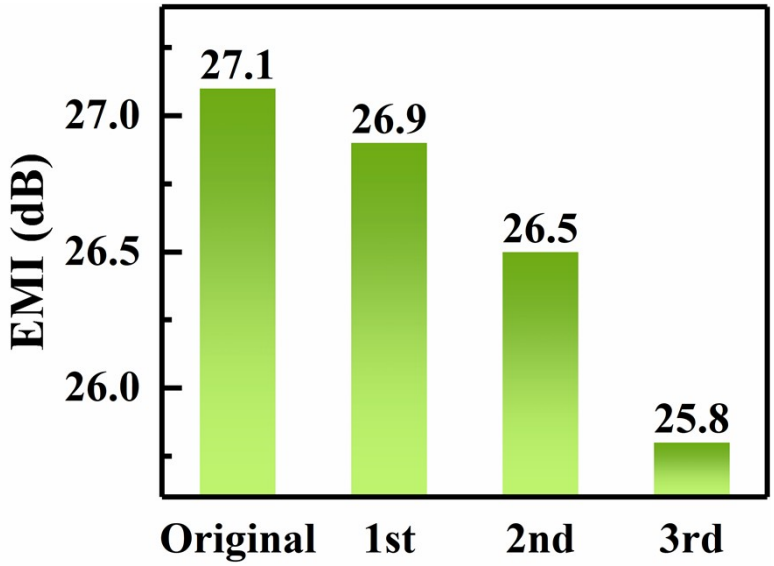

Figure S12 Average EMI SE of AgNW-MXene/PU-$DMBA_{0.25}$ TCF after multiple cut-off/healing cycles.

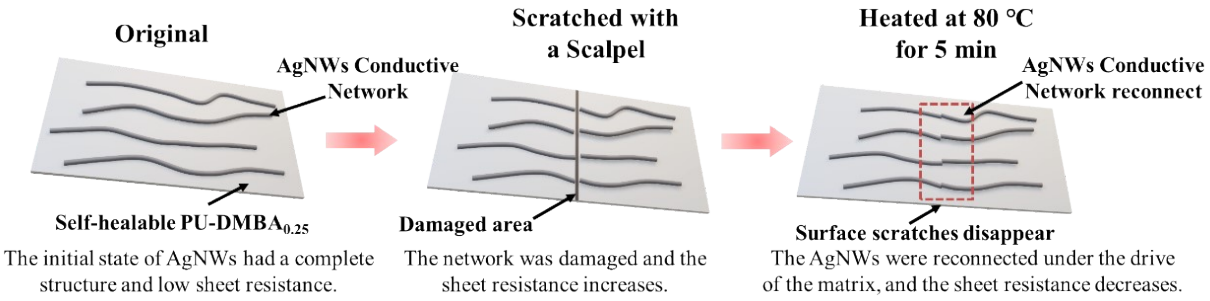

Figure S13 Schematics illustrations of the proposed self-healing mechanism for AgNW-MXene/PU-DMBA$_{0.25}$ TCFs.

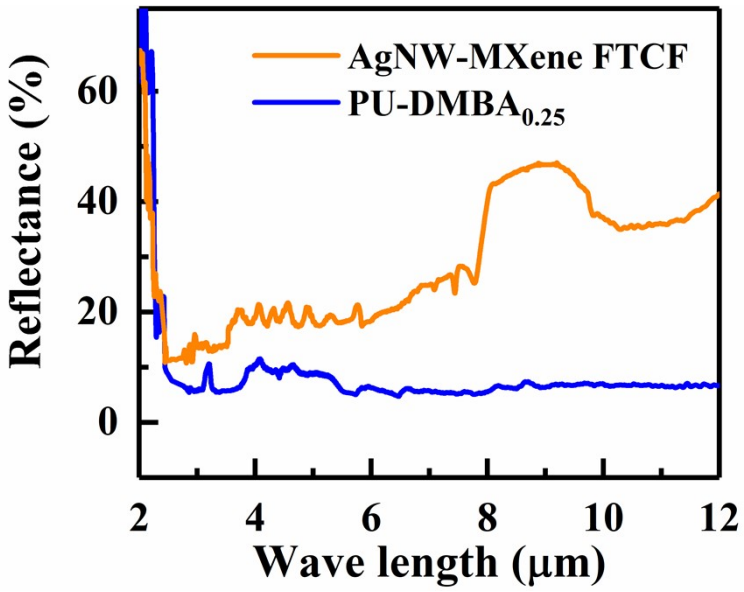

Figure S14 Reflectance of the PU-DMBA$_{0.25}$ and AgNW-MXene/PU-DMBA$_{0.25}$ TCFs.

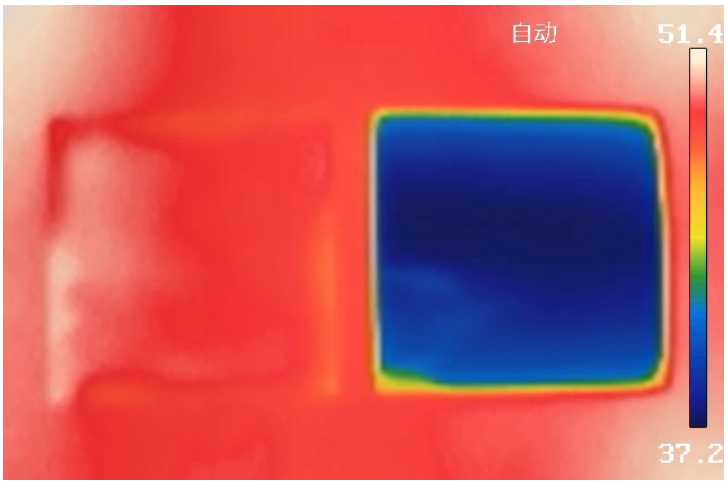

Figure S14 IRT photograph of PU-DMBA$_{0.25}$ (left) and AgNW-MXene/PU-DMBA$_{0.25}$ TCF (right).

Compared to the 11.5% of the PU-DMBA$_{0.25}$, the mid-IR reflectivity increases to 51 % after AgNW-MXene coating. This suggests a high mid-IR blocking for the AgNW-MXene/PU-DMBA$_{0.25}$ TCF. The thermal image results of the two films heated simultaneously on the heating table shows that the PU matrix has a high emissivity, while the composite film has a low emissivity, proving that the prepared TCF has a good thermal insulation effect and has great potential for use in the field of thermal management.

Table S5. Comparison of optoelectronic properties, mechanical properties, self-healing ability, and EMI properties of various flexible transparent conductive materials.

	Materials	Substrate	Tensile strength (MPa)	Transmittance (%)	EMI SE (dB)	Electrical Conductivity	Self-healing efficiency of conductivity (%)	Ref
Composite conductive Materials	AgNW-MXene	PU	24.4	82.8	27.1	18 Ω/sq	99.2	This work
	AgNW	PU	0.28	~ 85	~10	~ 20.41 Ω/sq	~100	[1]
				~ 82	~20.1	~ 6.79 Ω/sq		
				~ 77.4	~31.0	~ 4.58 Ω/sq		
				~ 70	~34.0	~ 2.31 Ω/sq		
				~ 60	>39	~ 1.70 Ω/sq		
	AgNW	D-A based polymer	Not given	58	/	9.5 Ω/sq	Not given	[2]
				50	/	18.6 Ω/sq	97.0	
		Zn–Bpy–PDMS	0.9	86.6	/	76.2 Ω/sq	Not given	[3]
				81.4	/	70.4 Ω/sq		
				77.1	/	18.3 Ω/sq		
	CuNW	DA-PU	/	66.5	/	22.3 Ω/sq	98.0	[4]
	AgNW/MXene	PET	/	81.96	/	12.09 ± 1.28 Ω/sq	/	[5]
				81.85	/	11.20 ± 3.83 Ω/sq		
				81.58	/	10.79 ± 2.39 Ω/sq		

				82.84	/	10.91 ± 1.03 Ω/sq		
				80.56	/	12.72 ± 2.67 Ω/sq		
	MXene grid/AgNW	PET	/	83	19.1	50.9 Ω/sq	/	[6]
				81	24.6	17.9 Ω/sq		
				72	32.5	6.7 Ω/sq		
	MXene/ AgNW/PEDOT-PET	PET	/	81.1	/	29.9 Ω/sq	/	[7]
				77.9	/	18.4 Ω/sq		
				75.2	/	12.9 Ω/sq		
	rGo/AgNW	PET	/	86.8	18.38	28.3 Ω/sq	/	[8]
				84.2	24.38	12.4 Ω/sq		
				81.9	33.62	4.7 Ω/sq		
Intrinsically conductive Material	PVDF-*co*-HFP	/	~ 0.1	92	/	7.06×10^{-5} S/cm	95.35	[9]
	Poly (AAm/ChCl-*co*-MA/ChCl)	/	~ 0.3	95.1	/	4.0×10^{-4} S/cm	94.0	[10]
	ChCl+AA+$AlCl_3{\cdot}6H_2O$	/	~ 6	~92	/	10.29×10^{-4} S/cm	~82.8%	[11]
			~ 5	~ 93	/	~ 9.5×10^{-4} S/cm		
			~ 2.5	~ 94	/	~ 8.3×10^{-4} S/cm		
			~ 1	~ 93	/	6.64×10^{-4} S/cm		
	Poly (PDES)-PA	/	~ 0.45	93	/	7.8×10^{-4} S/cm	91.5	[12]

PDA–clay–PSBMA	/	0.08	/	/	0.02 S/m	97.6	[13]
(LiTFSI)+butyl acrylate	/	0.25	92.4	/	1.27×10^{-4} S/cm	/	[14]
4-acryloylmorpholine+propylene carbonate	/	0.05	93	/	7.9×10^{-4} S/cm	/	[15]

References

1. F. Sun, J. Xu, T. Liu, F. Li, Y. Poo, Y. Zhang, R. Xiong, C. Huang and J. Fu, *Mater Horiz*, 2021, **8**, 3356-3367.
2. C. Gong, J. Liang, W. Hu, X. Niu, S. Ma, H. T. Hahn and Q. Pei, *Advanced Materials*, 2013, **25**, 4186-4191.
3. G. Ye, Z. Song, T. Yu, Q. Tan, Y. Zhang, T. Chen, C. He, L. Jin and N. Liu, *ACS applied materials & interfaces*, 2019, **12**, 1486-1494.
4. X. Zhang, Z. Tang, D. Tian, K. Liu and W. Wu, *Materials Research Bulletin*, 2017, **90**, 175-181.
5. W. Chen, R. Zhang, X. Yang, H. Wang, H. Yang, X. Hu and S. Zhang, *Journal of Materials Chemistry C*, 2022, **10**, 8625-8633.
6. M. Jin, W. Chen, L.-X. Liu, H.-B. Zhang, L. Ye, P. Min and Z.-Z. Yu, *Journal of Materials Chemistry A*, 2022, **10**, 14364-14373.
7. Y. Wang, Y. Liu, T. Wang, S. Liu, Z. Chen and S. Duan, *Nanotechnology*, 2022, **33**, 455201.
8. G. Wang, Y. Zhao, F. Yang, Y. Zhang, M. Zhou and G. Ji, *Nano-Micro Letters*, 2022, **14**, 1-14.
9. Y. Cao, T. G. Morrissey, E. Acome, S. I. Allec, B. M. Wong, C. Keplinger and C. Wang, *Advanced Materials*, 2017, **29**, 1605099.
10. R. a. Li, T. Fan, G. Chen, K. Zhang, B. Su, J. Tian and M. He, *Chemistry of Materials*, 2020, **32**, 874-881.
11. Q. Zhang, G. Chen, L. Lin and M. He, *Polymer Chemistry*, 2021, **12**, 2016-2023.
12. T. Fan, G. Chen, H. Xie, B. Su and M. He, *Chemical Engineering Journal*, 2020, **393**, 124685.
13. X. Pei, H. Zhang, Y. Zhou, L. Zhou and J. Fu, *Materials Horizons*, 2020, **7**, 1872-1882.
14. L. Shi, T. Zhu, G. Gao, X. Zhang, W. Wei, W. Liu and S. Ding, *Nature communications*, 2018, **9**, 1-7.
15. Y. Gao, L. Shi, S. Lu, T. Zhu, X. Da, Y. Li, H. Bu, G. Gao and S. Ding, *Chemistry of Materials*, 2019, **31**, 3257-3264.